arXiv:1401.1178v2 [cond-mat.mes-hall] 3 Jul 2014

High-performance solution of the transport problem in a graphene armchair structure with a generic potential

Demetrio Logoteta* and Paolo Marconcini
Dipartimento di Ingegneria dell'Informazione, Università di Pisa, Via Caruso 16, I-56122 Pisa, Italy.

Claudio Bonati
Dipartimento di Fisica, Università di Pisa and INFN, Largo Pontecorvo 3, I-56127 Pisa, Italy.

Maurizio Fagotti
The Rudolf Peierls Centre for Theoretical Physics, University of Oxford - Oxford OX1 3NP, UK.

Massimo Macucci†
Dipartimento di Ingegneria dell'Informazione, Università di Pisa, Via Caruso 16, I-56122 Pisa, Italy.

We propose an efficient numerical method to study the transport properties of armchair graphene ribbons in the presence of a generic external potential. The method is based on a continuum envelope-function description with physical boundary conditions. The envelope functions are computed in the reciprocal space, and the transmission is then obtained with a recursive scattering matrix approach. This allows a significant reduction of the computational time with respect to finite difference simulations.

I. INTRODUCTION

Graphene, a two-dimensional hexagonal lattice of carbon atoms isolated in 2004 by Geim and Novoselov [1], represents a very interesting material in several fields of science and technology. Since its low-energy properties can be described by a Dirac equation, it is considered to be an ideal test bed for the investigation of relativistic effects at non-relativistic velocities [2]. Moreover, its unique properties make it suitable for applications in many different fields of technology [3]. Its atomic thickness and high room-temperature mobility, for example, make it a candidate material for postsilicon electronics.

For applications in digital electronics the presence of a sufficiently large energy gap is fundamental [4]. A gap can be induced by the lateral confinement in narrow ribbons with a transverse size of a few nanometers or of tens of nanometers, which can be efficiently modeled with atomistic techniques, such as tight-binding approaches. Fabrication of such nanowires is, however, very challenging, and therefore also alternative and/or complementary approaches to open up a gap are being pursued, such as the usage of bilayer graphene [5–8], of chemical functionalization [9–12], and of doping [13–16]. Large graphene devices (with a size of several hundreds of nanometers or of microns) can, however, be convenient (or mandatory) in radio-frequency or sensor applications, which do not necessarily require an energy gap [17–22]. In these cases an atomistic analysis is not feasible, since it is numerically too expensive, and more approximate techniques (such as envelope-function descriptions) have to be adopted. The availability of techniques suitable for the simulation of large-area graphene structures is also essential for a direct comparison with transport and noise measurements performed on micron-sized flakes (see for example Refs. [23–26]).

Numerical efficiency is particularly important for transport calculations, which are usually self-consistently coupled with the solution of the Poisson equation, and therefore typically need hundreds or thousands of iterations to reach global convergence. As a consequence, numerical performance can often make the difference between a feasible calculation and a computationally impossible task. For this reason, it is important to develop reliable algorithms that are more approximate but more efficient than the atomistic ones.

A continuum approach has been often used for the numerical simulation of transport in ribbons made up of transverse regions with constant potential [27–29], for which analytical expressions for the wave function in each region are available [30–32]. However, for a generic potential, the envelope function equation (which is a Dirac equation) has to be solved numerically, and the relativistic dispersion relation introduces some complications in the standard discretization schemes.

In order to avoid these difficulties, the first numerical studies [33, 34] adopted a momentum space regularization of the Dirac equation. For ribbons with a large aspect ratio, such as those studied in Refs. [33, 34], the boundary conditions are expected to be largely uninfluential and thus periodic boundary conditions were used. Tworzidło *et al.* [35] later performed a real-space transport analysis of large aspect ratio graphene ribbons by adopting the Stacey discretization scheme [36, 37]. More recently, Hernández *et al.* [38] studied the transport properties of zigzag and armchair ribbons in the direct space, with physical boundary conditions. For the zigzag rib-

* Present address: IMEP-LAHC, Grenoble INP-Minatec, 3 Parvis Louis Néel, 38016 Grenoble Cedex 1, France.
† Corresponding author: m.macucci@mercurio.iet.unipi.it

bon, in the transverse direction they adopted the discretization by Susskind [39] and in the longitudinal direction the discretization by Stacey; for the armchair ribbon they used the Stacey discretization in both directions. Snyman *et al.* [40] previously adopted the alternative method of mapping the Dirac equation onto a Chalker-Coddington network model [41], which in the past was used to describe percolation in disordered samples in the quantum Hall effect [42–44].

After the seminal contributions by Bardarson *et al.* [33] and by Nomura *et al.* [34] the attention of the graphene community mainly focused on the finite difference methods, for which the physical boundary conditions can be easily implemented [45]. In this paper we will show how to extend the reciprocal space algorithm to the case of armchair boundaries, and we will present compelling evidence that this method is numerically much more efficient than the finite difference schemes.

For the solution of the transport problem we will adopt a scattering-matrix approach. The ribbon is partitioned into a series of thin slices in the direction along the current flow (which we will refer to as the longitudinal direction). In each slice the potential is approximated with a longitudinally constant function, and the Dirac eigenvalue problem is solved in the Fourier transformed space. The conductance of the whole structure is then evaluated applying a mode-matching procedure at the interfaces between adjacent slices.

The paper is organized as follows. In Sec. II we introduce the $\vec{k}\cdot\vec{p}$ approximation for graphene ribbons and present the equations that describe the transverse slices of the device. In order to perform a comparison with the approach we have decided to adopt, in Sec. III we outline a few finite-difference techniques that could be employed to solve the envelope function equation in the direct space. In Sec. IV we introduce a mapping of the armchair problem into one with periodic boundary conditions and in Sec. V we provide a detailed discussion of the reciprocal space technique used in Ref. [46], where numerical precision was crucial. In Sec. VI we compare the numerical efficiency of the methods in the direct and reciprocal space. Section VII is devoted to the solution of the two-dimensional transport problem for an armchair graphene ribbon in the realistic situation of a potential that varies also in the longitudinal direction.

II. THE NUMERICAL PROBLEM

The wave function of graphene can be approximated by means of a linear combination of the $2p^z$ orbitals of the carbon atoms of its two inequivalent sublattices (see, e.g., Refs. [30, 32, 47]). Using the subscripts A and B to distinguish the quantities associated with different sublattices, the wave function is written as

$$\psi(\vec{r}) = \sum_{\vec{R}_A} \psi_A(\vec{R}_A)\varphi(\vec{r}-\vec{R}_A) + \sum_{\vec{R}_B} i\,\psi_B(\vec{R}_B)\varphi(\vec{r}-\vec{R}_B)\,, \tag{1}$$

where the sums are over the atom positions, and $\varphi(\vec{r})$ is the $2p^z$ orbital.

We consider an armchair ribbon with N_D dimer lines of carbon atoms across its width. The distance between the opposite edges is $W = (N_D-1)\,a/2$, where $a = \sqrt{3}a_{C-C}$ is the graphene lattice constant and $a_{C-C} \simeq 0.142$ nm is the distance between nearest-neighbor atoms. We denote by x and y the longitudinal and transverse directions, respectively; the Dirac points $\vec{K}$ and $\vec{K}'$ can be expressed as $\vec{K} = -K\hat{y}$ and $\vec{K}' = K\hat{y}$, with $K = 4\pi/(3a)$.

For large enough N_D and a potential that is slowly varying on the lattice scale, atomistic details can be disregarded and the low-energy physics can be described by means of a $\vec{k}\cdot\vec{p}$ approximation. This is achieved in practice by promoting the coefficients $\psi_A(\vec{R}_A)$ and $\psi_B(\vec{R}_B)$ in (1) to continuous functions of the position $\vec{r}$ and by writing the functions $\psi_A(\vec{r})$ and $\psi_B(\vec{r})$ in terms of four envelope functions F as (see, e.g., Refs. [30, 32, 47])

$$\psi_\beta(\vec{r}) = e^{i\vec{K}\cdot\vec{r}}F_\beta^{\vec{K}}(\vec{r}) - i\,e^{i\vec{K}'\cdot\vec{r}}F_\beta^{\vec{K}'}(\vec{r})\,, \tag{2}$$

where $\beta = A, B$.

It can be shown (see, e.g., Refs. [30, 32, 47]) that the envelope functions satisfy the massless Dirac equation

$$\begin{aligned} -i\gamma(\partial_x\sigma_x + \partial_y\sigma_y)\vec{F}^{\vec{K}} &= E\vec{F}^{\vec{K}} \\ -i\gamma(\partial_x\sigma_x - \partial_y\sigma_y)\vec{F}^{\vec{K}'} &= E\vec{F}^{\vec{K}'}\,, \end{aligned} \tag{3}$$

where

$$\vec{F}^{\vec{\alpha}} = \begin{bmatrix} F_A^{\vec{\alpha}}(\vec{r}) \\ F_B^{\vec{\alpha}}(\vec{r}) \end{bmatrix} \tag{4}$$

(with $\vec{\alpha} = \vec{K}, \vec{K}'$), $\partial_x = \partial/\partial x$, $\partial_y = \partial/\partial y$, σ_x, σ_y are Pauli matrices, E is the total energy of a particle in the ribbon, and $\gamma = (\sqrt{3}/2)\gamma_0 a \equiv v_F\hbar$. The constant $\gamma_0 \simeq 2.7$ eV is the modulus of the transfer integral between nearest-neighbor carbon atoms, v_F is the Fermi velocity of graphene, and $\hbar$ is the reduced Planck constant. Within the $\vec{k}\cdot\vec{p}$ approximation, the presence of an external electric field is handled by introducing the potential energy $U(\vec{r})$ into Eq. (3):

$$\begin{aligned} [-i\gamma(\partial_x\sigma_x + \partial_y\sigma_y) + U(\vec{r})I]\vec{F}^{\vec{K}} &= E\vec{F}^{\vec{K}} \\ [-i\gamma(\partial_x\sigma_x - \partial_y\sigma_y) + U(\vec{r})I]\vec{F}^{\vec{K}'} &= E\vec{F}^{\vec{K}'}\,, \end{aligned} \tag{5}$$

where I is the 2×2 identity matrix.

Dirichlet boundary conditions for the wave function ψ have to be imposed on the two dimer lines just outside the ribbon, at a distance $a/2$ from the ribbon edges, where passivation approximately takes place. We choose the origin of the y axis in such a way that these dimer lines

are identified by the conditions $y = 0$ and $y = \tilde{W} \equiv W + a$. The vanishing of the wave function on the passivation lines leads to the boundary conditions [30–32]

$$\psi_\beta(x, y = 0) = \psi_\beta(x, y = \tilde{W}) = 0 \tag{6}$$

for both sublattices ($\beta = A, B$).

In a waveguide-like configuration in which the potential energy U depends only on the transverse coordinate y, the longitudinal component of the momentum is constant; we will denote the longitudinal wave vector by κ_x. The envelope functions that solve the Dirac equation (5) can be decomposed into a propagating wave along x and a confined component in the transverse direction:

$$F^{\vec{\alpha}}_\beta(\vec{r}) = e^{i\kappa_x x}\Phi^{\vec{\alpha}}_\beta(y) \tag{7}$$

($\vec{\alpha} = \vec{K}, \vec{K}'$; $\beta = A, B$). The functions $\Phi^{\vec{\alpha}}_\beta$ thus satisfy (*cf.* Eq. (5))

$$\begin{aligned}\left[\sigma_x f(y) + \sigma_z \frac{d}{dy}\right]\vec{\varphi}^{\vec{K}}(y) &= -\kappa_x \vec{\varphi}^{\vec{K}}(y)\\ \left[\sigma_x f(y) - \sigma_z \frac{d}{dy}\right]\vec{\varphi}^{\vec{K}'}(y) &= -\kappa_x \vec{\varphi}^{\vec{K}'}(y)\,,\end{aligned} \tag{8}$$

where we introduced the shorthands

$$\vec{\varphi}^{\vec{K}}(y) = \begin{bmatrix}\Phi^{\vec{K}}_A(y)\\ \Phi^{\vec{K}}_B(y)\end{bmatrix}, \quad \vec{\varphi}^{\vec{K}'}(y) = \begin{bmatrix} i\,\Phi^{\vec{K}'}_A(y)\\ i\,\Phi^{\vec{K}'}_B(y)\end{bmatrix}, \tag{9}$$

and $f(y) = [U(y) - E]/\gamma$.

The boundary conditions (6) become

$$\begin{aligned}\vec{\varphi}^{\vec{K}}(0) &= \vec{\varphi}^{\vec{K}'}(0)\\ \vec{\varphi}^{\vec{K}}(\tilde{W}) &= e^{2iK\tilde{W}}\vec{\varphi}^{\vec{K}'}(\tilde{W}) = e^{-i\eta\frac{2\pi}{3}}\vec{\varphi}^{\vec{K}'}(\tilde{W})\end{aligned} \tag{10}$$

where

$$N_D + 1 \equiv \eta \mod 3 \tag{11}$$

and $\eta \in \{-1, 0, 1\}$. In particular, if $N_D + 1 = 3M + \eta$ (with M an integer), we have

$$2K\tilde{W} = 2\pi(2M + \eta) - \eta\frac{2\pi}{3} \equiv 2\pi n_0 - \eta\frac{2\pi}{3}\,. \tag{12}$$

The introduction of the discrete variable η is convenient since the product $K\tilde{W}$ can be very large in the case of wide ribbons, where the envelope-function approximation is expected to be more reliable. In fact, η is a geometrical property of the lattice structure that goes beyond the $\vec{k}\cdot\vec{p}$ approximation.

It is important to notice that although the envelope functions associated with different Dirac points decouple in the differential equations (8), they are in fact mixed by the boundary conditions (10). This coupling makes it nontrivial to define a symmetric discretization of (8).

As previously noted, in the presence of a generic external electric field the differential eigenproblem (8)-(10) cannot be solved analytically: it is necessary to rely on numerical methods in order to obtain approximate expressions for the transverse components Φ of the envelope functions and the corresponding longitudinal wave vectors κ_x.

III. FINITE DIFFERENCE METHODS

In this section we describe a few finite difference techniques that could be adopted to numerically solve Eqs. (8)-(10) in the direct space.

In a finite difference approach the unknowns are the values of the functions Φ on a grid of N_y points along the effective width $\tilde{W}$ of the ribbon; here we assume a uniform grid, by setting $y_i = (i-1)\Delta_y$, with $\Delta_y = \tilde{W}/(N_y - 1)$ and $i = 1, \ldots, N_y$. The derivatives are expressed as linear combinations of the values of the Φ on a finite number of grid points, and the boundary conditions are constraints that reduce the number of unknowns. As a consequence, the system of equations (8) is mapped to an algebraic eigenvalue problem $A\,\vec{v} = -\kappa_x\,\vec{v}$, where the elements of the vector $\vec{v}$ are the values of the Φ at the grid points and the eigenvalues give the longitudinal wave vectors κ_x.

In general, as Δ_y approaches zero, a subset of eigenvectors of A, together with their respective eigenvalues, converge to the solutions of Eq. (8). The remaining eigenvectors and eigenvalues are discretization artifacts that have no meaningful continuum limit. We will refer to them as spurious solutions.

The adopted discretization scheme affects both the numerical efficiency and the appearance of spurious solutions. We now discuss the implications of the simplest discretization schemes:

(a) Naive asymmetric discretization

(b) Naive symmetric discretization

(c) Improved symmetric discretization.

In scheme (a) the first differential equation of (8) is evaluated at the points y_i with $i = 1, \ldots, N_y - 1$ and the second differential equation of (8) at y_i with $i = 2, \ldots, N_y$. Different representations for the derivatives are used: in the first equation the two-point forward discretization formula $(d\Phi/dy)|_{y_i} \simeq [\Phi(y_{i+1}) - \Phi(y_i)]/\Delta_y$ is used and in the second one the two-point backward discretization formula $(d\Phi/dy)|_{y_i} \simeq [\Phi(y_i) - \Phi(y_{i-1})]/\Delta_y$. The differential equations (8) are thus mapped to a $4\,(N_y - 1) \times 4\,(N_y - 1)$ eigenvalue problem. We have also considered the alternative scheme of a symmetric discretization formula inside the ribbon and an asymmetric one at the edges. In both cases a very slow convergence is observed. Moreover, a large number of spurious solutions are obtained, which persist also when higher order discretization schemes are used.

As an example, in Fig. 1 we show the eigenvalues κ_x obtained for $U(y) = 0$ using a three-point discretization formula, symmetric inside the ribbon and asymmetric at the edges. This problem is analytically solvable, and the exact values of κ_x turn out to be either real or purely imaginary (see, e.g., Refs. [30, 32]). The discretized problem instead also has a large number of complex solutions with nonzero real and imaginary parts (see Fig. 1). In

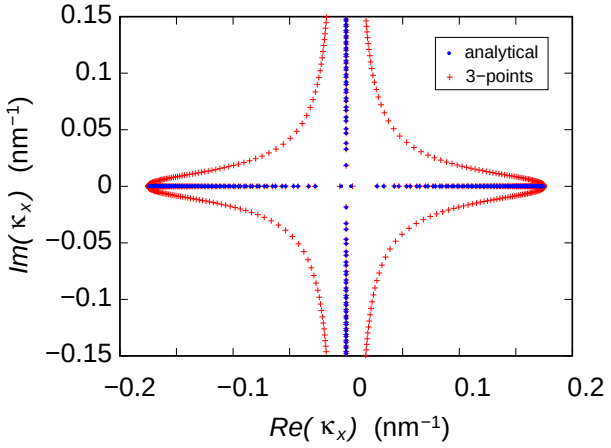


FIG. 1. (Color online) Eigenvalues κ_x for a graphene nanoribbon with 8131 dimer lines (≈ 1 μm wide) and null potential energy, for a Fermi energy of 0.1 eV. The analytical results are compared with those obtained with a standard three-point discretization scheme (symmetric inside the ribbon and asymmetric at the edges), using a large number of discretization points (5000) along the ribbon width.

this simple case we can identify them as spurious solutions. However, for a generic potential energy function $U(y)$, complex solutions can be physical [46], so they cannot be rejected *a priori*. If, instead of a three-point formula, we use, for example, a five-point formula for the spatial discretization, the nonspurious eigenvalues converge onto the exact eigenvalues more quickly, as the discretization step is reduced, but the same number of spurious eigenvalues are present.

In scheme (b) the grid is modified to have a symmetric discretization in every point of the grid. Defining $y_0 = -\Delta_y$ and $y_{N_y+1} = W + \Delta_y$, the original boundary conditions (10) can be replaced with the relations

$$\begin{aligned} \vec{\varphi}^{\vec{K}}(y_0) &= \vec{\varphi}^{\vec{K}'}(y_1) \\ \vec{\varphi}^{\vec{K}'}(y_0) &= \vec{\varphi}^{\vec{K}}(y_1) \\ \vec{\varphi}^{\vec{K}}(y_{N_y+1}) &= e^{-i\eta\frac{2\pi}{3}}\,\vec{\varphi}^{\vec{K}'}(y_{N_y}) \\ \vec{\varphi}^{\vec{K}'}(y_{N_y+1}) &= e^{i\eta\frac{2\pi}{3}}\,\vec{\varphi}^{\vec{K}}(y_{N_y})\,, \end{aligned} \tag{13}$$

which reduce to (10) in the continuum limit. Derivatives in (8) are evaluated by using the symmetric three-point discretization $(d\Phi/dy)|_{y_i} \simeq [\Phi(y_{i+1}) - \Phi(y_{i-1})]/(2\,\Delta_y)$ in all the points y_i of the grid ($i = 1, \ldots, N_y$) and the differential equations are thus mapped into a $(4\,N_y) \times (4\,N_y)$ eigenvalue problem.

The eigenvalues of the discretized problem turn out to be always double degenerate. In detail, each eigenspace is the span of two vectors, let us say $\vec{v}_{(c)}$ and $\vec{v}_{(l)}$, such that the components of $\vec{v}_{(l)}$ exhibit even-odd oscillations, while the others have oscillation frequency almost independent of N_y. The eigenvector $\vec{v}_{(l)}$ cannot have a continuum counterpart, hence the double degeneracy is in fact a lattice artefact.

This is a clear manifestation of the so-called fermion doubling problem: a "naive" direct space discretization of the Dirac equation results in the appearance of 2^d fermions (instead of one) in d space dimensions (in our case $d = 1$); this is an infrared effect, i.e. it does not disappear in the continuum limit $\Delta_y \to 0$. The fermion doubling is a very well known problem in the field of lattice quantum chromodynamics (see, e.g., Refs. [48, 49]) and is deeply connected with the chiral anomaly (see, e.g., Ref. [50]), i.e. with the impossibility of regularizing a theory with massless fermions in a local, chiral symmetric way. In our simple case, it is caused by the symmetric three-point discretization formula for the derivative, which involves an incremental step of $2\,\Delta_y$, and hence decouples odd and even grid points.

Many methods have been developed to overcome the fermion doubling problem; in scheme (c) we employ the method proposed in Refs. [36, 37], which has a quite simple implementation and was already applied in Ref. [35]. The idea is to use a symmetric three-point discretization formula for the derivative, but with an incremental step equal to Δ_y instead of $2\,\Delta_y$. This can be done by evaluating the differential equations on an auxiliary grid, with nodes at the center coordinates $y_{i+(1/2)}$ of the cells of the original grid: $y_{i+(1/2)} = (y_i + y_{i+1})/2$, for $i = 1, \ldots, N_y - 1$. The derivative is then approximated by $(d\Phi/dy)|_{y_{i+(1/2)}} \simeq [\Phi(y_{i+1}) - \Phi(y_i)]/\Delta_y$. The potential energy $U(y)$ is known for every value of y and can be directly evaluated at $y_{i+(1/2)}$, while the value of the functions Φ at $y_{i+(1/2)}$ can be estimated by the average of the values at y_i and y_{i+1}: $\Phi(y_{i+(1/2)}) \simeq [\Phi(y_i) + \Phi(y_{i+1})]/2$.

The original differential equations (8) are thus mapped into the generalized algebraic eigenproblem $A\,\vec{v} = -\kappa_x\,B\,\vec{v}$, with A and B that are $4\,(N_y - 1) \times 4\,(N_y - 1)$ matrices. Since the matrix B is invertible, this problem is in fact equivalent to the standard eigenproblem $(B^{-1}\,A)\,\vec{v} = -\kappa_x\,\vec{v}$. We notice, however, that while A and B are sparse matrices, $B^{-1}A$ is dense. As a consequence, optimized methods to solve sparse eigenproblems (like the Arnoldi methods) cannot be directly applied to the standard form. The sparsity of A and B can, however, still be exploited in the multiplication $\vec{y} = B^{-1}\,A\vec{x}$, which is the fundamental operation to be performed. This can be done by carrying out first the multiplication by a sparse matrix $\vec{z} = A\vec{x}$ and then solving a sparse linear system $B\vec{y} = \vec{z}$. This discretization scheme solves the problems of schemes (b) and (c): there are neither spurious eigenvalues nor unphysical double degeneracies.

In the next sections we will show that this is not the most efficient way to solve the system of differential equations (8).

IV. REFORMULATION AS A PROBLEM WITH PERIODIC BOUNDARY CONDITIONS

The numerical techniques in the real domain that we described in Sec. III do not enable an efficient numerical analysis of the problem (8)-(10): in order to obtain high precision results, very large matrices have to be diagonalized, and the size soon becomes prohibitive. In this section we reformulate the problem (8)-(10) on a different domain, but with periodic boundary conditions. In the next section we will show how to solve the resulting numerical problem in the reciprocal space.

We define the two-component function $\vec{\varphi}(y)$ by

$$\vec{\varphi}(y) = \begin{cases} \vec{\varphi}^{\vec{K}}(y) & y \in [0, \tilde{W}] \\ e^{-i\eta\frac{2\pi}{3}}\vec{\varphi}^{\vec{K}'}(2\tilde{W} - y) & y \in [\tilde{W}, 2\tilde{W}]\,. \end{cases} \tag{14}$$

From the second of the boundary conditions (10) we see that $\vec{\varphi}$ is continuous in its whole domain, while the first condition gives

$$e^{-i\eta\frac{2\pi}{3}}\vec{\varphi}(0) = \vec{\varphi}(2\tilde{W})\ . \tag{15}$$

Equation (15) can be interpreted as the requirement of $2\tilde{W}$ periodicity for the function $\exp[i\eta\pi y/(3\tilde{W})]\vec{\varphi}(y)$.

The differential equation satisfied by $\vec{\varphi}$ can be easily deduced from Eq. (8) and can be written in the compact form

$$\begin{gathered} \left[\frac{d}{d\,y}\sigma_z + h(y)\sigma_x\right]\vec{\varphi}(y) = -\kappa_x\vec{\varphi}(y) \\ e^{i\eta\frac{2\pi}{3}}\vec{\varphi}(2\tilde{W}) = \vec{\varphi}(0)\,, \end{gathered} \tag{16}$$

where

$$h(y) = f(\tilde{W} - |\tilde{W} - y|) \qquad y \in [0, 2\,\tilde{W}]\,. \tag{17}$$

In this way we have halved the number of first-order differential equations by doubling the solution domain. From Eq. (16) we see that κ_x is an eigenvalue of the system [with corresponding eigenfunction $\vec{\varphi}_{\kappa_x}(y)$], if and only if $-\kappa_x$, κ_x^* and $-\kappa_x^*$ are eigenvalues, as well. The corresponding eigenfunctions can be expressed in terms of the eigenfunction of κ_x:

$$\begin{aligned} \vec{\varphi}_{-\kappa_x}(y) &\propto \sigma_y\,\vec{\varphi}_{\kappa_x}(y) \\ \vec{\varphi}_{\kappa_x^*}(y) &\propto \sigma_x\left[\vec{\varphi}_{\kappa_x}(2\tilde{W} - y)\right]^* \\ \vec{\varphi}_{-\kappa_x^*}(y) &\propto \sigma_z\left[\vec{\varphi}_{\kappa_x}(2\tilde{W} - y)\right]^*\,. \end{aligned} \tag{18}$$

It can be shown [46] that there is no degeneracy when $\eta = \pm 1$, i.e. when $N_D + 1$ is not divisible by three, while this is not generally true for $\eta = 0$. We also note that the solutions of the problems with $\eta = -1$ and $\eta = +1$ can be mapped into each other by the relation

$$\vec{\varphi}_{k_x}^{(\eta=-1)}(y) = \sigma_x\vec{\varphi}_{k_x}^{(\eta=1)}(2\tilde{W} - y)\,. \tag{19}$$

Solutions with non-real κ_x^2 (i.e. κ_x with nonzero real and imaginary parts) can be found in the presence of an external electric field. Their appearance is related to the existence of exceptional points, i.e. points in which the operator in Eq. (16) is not diagonalizable (notice that the operator is not self-adjoint). The existence of nonreal κ_x^2 values is a manifestation of the $\mathcal{PT}$ symmetry breaking in the system [46].

The methods described in the previous section [in particular, scheme (c)] could also be used to solve problem (16). However, we did not observe any significant efficiency gain with respect to the discretization of the original differential problem.

In the Appendix we show that Eq. (16) can be recast into the form of a complex second-order differential equation for a scalar unknown function. In that form the discretization in direct space is free from fermion doubling effects. We did not actively investigate its numerical solution, since the method that we are going to describe in the next section turns out to be much more efficient than the direct space ones [51].

V. SOLUTION IN THE RECIPROCAL SPACE

A key feature of the discretization in the direct space (discussed in Sec. III) was the representation of the derivative.

Let us consider a uniform grid with node spacing a and the n-point discretization on it of the first derivative $\phi'(p)$ of a generic function ϕ, computed at point p. This discretization is constructed by Taylor expanding $\phi(p + ia)$ for different values of the integer i and finding the linear combination of these expansions that is equal to $a\phi'(p)$ up to $a^n\phi^{(n)}(p)$ corrections. If the function ϕ is smooth, the discretization error of the $n-$point derivative is thus $\mathcal{O}(a^{n-1})$ for every n. However, if the αth order derivative of ϕ in p is discontinuous, we cannot improve the precision of the discretization for $n > \alpha$ without introducing coefficients that depend on the specific function ϕ itself. As a consequence, the discretization error of a generic $n-$point discretization of the derivative scales as

$$|\phi'(p) - \phi'_{(N_y)}(p)| \gtrsim \mathcal{O}(N_y^{1-\min(\alpha,n)})\,, \tag{20}$$

where $\phi'_{(N_y)}(p)$ is the n-point discretization of the first derivative on a grid with N_y points.

In the specific case (16), it is enough that the first derivative of the potential is nonzero at the boundaries (i.e., the external electric field has a nonzero transverse component at the edges) for the second derivative of the eigenfunctions to be discontinuous at $y = 0, \tilde{W}$ [see Eq. (17)]; if so, the accuracy of the approximation is independent of n for $n \geq 2$, and Eq. (20) represents a very severe limitation both for the precision and for the efficiency of the numerical solution.

The Fourier methods are better behaved in this respect. While the direct space methods involve a global

distortion of the dispersion relation, in the Fourier case the derivative is exactly reproduced for the frequencies lower than the cutoff. The fermion doubling problem is absent, as one can argue by tracing back its origin to the periodicity of the wave function across the Brillouin zone induced by the space discretization (a simple topological argument is given in Ref. [50], §13.1).

Since both $h(y)$ and $\exp[i\eta\pi y/(3\tilde{W})]\vec{\varphi}(y)$ (separately) assume the same value at 0 and $2\tilde{W}$, they can be extended by periodicity with period $2\tilde{W}$ without introducing discontinuities. We define their Fourier coefficients $h_\ell \equiv h_{-\ell}$ and $\vec{a}_m$ by

$$\begin{aligned} h(y) &= \sum_{\ell=-\infty}^{\infty} h_\ell e^{i\pi\ell y/\tilde{W}}\,, \\ \vec{\varphi}(y) &= \sum_{m=-\infty}^{\infty} \vec{a}_m e^{i\pi(m-\eta/3)y/\tilde{W}}\,. \end{aligned} \tag{21}$$

We substitute these expressions in the differential equation of (16) and then project onto the exponential functions $e^{i\pi(n-\eta/3)y/\tilde{W}}$; for the generic index n we obtain

$$\sum_{m=-\infty}^{+\infty} \left[i\frac{\pi}{\tilde{W}}\left(n-\frac{\eta}{3}\right)\sigma_z\delta_{n,m} + h_{n-m}\,\sigma_x \right] \vec{a}_m = -\kappa_x \vec{a}_n\,, \tag{22}$$

where $\delta_{n,m}$ is the Kronecker delta function. These equations are still exact and can be rewritten in the matrix form

$$M\vec{a} = -\kappa_x \vec{a} \tag{23}$$

where M is a structured infinite matrix whose 2×2 block is given by

$$M_{n,m} = P_n\delta_{n,m} + Q_{n,m} \tag{24}$$

with

$$P_n = i\frac{\pi}{\tilde{W}}\left(n-\frac{\eta}{3}\right)\sigma_z\,, \quad Q_{n,m} = h_{n-m}\,\sigma_x\,. \tag{25}$$

While the weight of the diagonal blocks P_n increases with $|n|$, Parseval's theorem [52] ensures that if $h(y)$ is square integrable the contribution of the blocks $Q_{n,m}$ vanishes for large values of $|n-m|$, i.e., sufficiently far from the principal diagonal of the matrix M. Actually, for the regular potentials for which the envelope function approach gives reliable results, the hypothesis of square integrability of $h(y)$ is a very weak assumption.

If we consider a sufficiently large positive integer D such that

$$\frac{\pi D}{\tilde{W}} \gg \max_j |h_j|\,, \tag{26}$$

the matrix M_0, with blocks $[M_0]_{n,m} = M_{n,m}$ and $|n|,|m| \le D$, contains the main information about the slowly varying solutions of (22): the Fourier coefficients that describe the low-frequency components of the spectrum are well approximated by those of the truncated problem [51]; the high-frequency components are instead negligible for the slow varying solutions. The finite dimensional problem $(M_0 + \kappa_x I)\vec{v}_0 = 0$ is not affected by doubling, since it is just a truncation of the original problem (22).

The eigenvalues of M_0 are accurate estimates of the longitudinal wave vectors κ_x. Each eigenfunction $\vec{\varphi}(y)$ can be reconstructed, using the corresponding eigenvector $\vec{a}_0$ of M_0, as

$$\vec{\varphi}(y) \approx \vec{\varphi}_D(y) \equiv \sum_{\mu=-D}^{D} [\vec{a}_0]_\mu\, e^{i\pi(\mu-\eta/3)y/\tilde{W}}\,. \tag{27}$$

Using (14) and (9), the transverse components Φ of the envelope functions are given by ($\beta = A, B$)

$$\begin{aligned} \Phi_\beta^{\vec{K}}(y) &\approx \sum_{\mu=-D}^{D} [a_0^\beta]_\mu\, e^{i\pi(\mu-\eta/3)y/\tilde{W}}\,, \\ \Phi_\beta^{\vec{K}'}(y) &\approx -i \sum_{\mu=-D}^{D} [a_0^\beta]_\mu\, e^{-i\pi(\mu-\eta/3)y/\tilde{W}}\,. \end{aligned} \tag{28}$$

Finally, from (2) and (7) it follows that

$$\psi_\beta(x,y) = 2\,i \sum_{\mu=-D}^{D} \left\{ [a_0^\beta]_\mu\, \sin[(\mu-n_0)\pi y/\tilde{W}] \right\} e^{i\kappa_x x}\,, \tag{29}$$

where n_0 has been defined in (12).

We explicitly note that, from the numerical point of view, all these computations strongly benefit from the use of optimized fast Fourier transform routines for the calculation of the Fourier series.

VI. NUMERICAL EFFICIENCY: COMPARISON AMONG METHODS

In this section we compare the numerical efficiency of the methods introduced so far, performing an analysis of the convergence rate for several test cases.

We are going to compare three main strategies:

- (S) method (c) of Sec. III
- (S_p) method (c) of Sec. III applied to the periodic problem (16)
- (F) the Fourier method described in Sec. V.

We consider a nanoribbon composed of $N_D = 4065$ dimer lines (corresponding to $\eta = 1$ and to an effective width $\tilde{W} \approx 500\,\mathrm{nm}$), with the following potentials (shown in Fig. 2):

(1) Step potential

$$U(y) = \begin{cases} 0\,\mathrm{eV} & y \le 200\,\mathrm{nm} \\ 0.2\,\mathrm{eV} & y > 200\,\mathrm{nm} \end{cases} \tag{30}$$

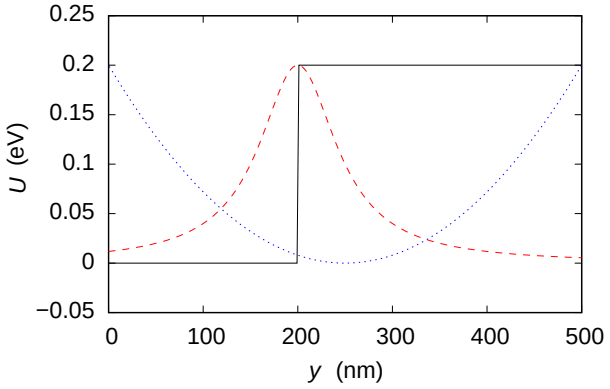


FIG. 2. (Color online) Plot of the potentials used to test the numerical efficiency of the methods: a step potential (solid curve), a Lorentzian potential (dashed curve), and a parabolic potential (dotted curve).

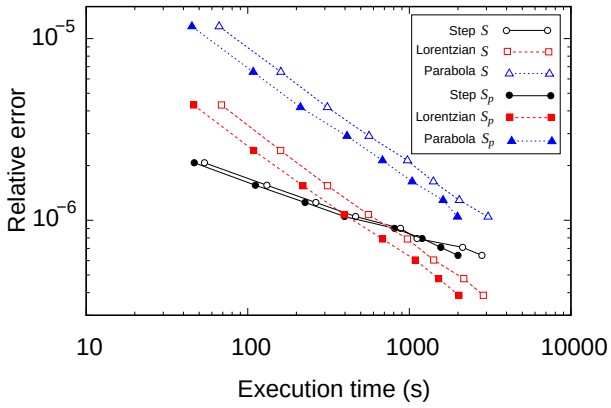


FIG. 3. (Color online) Relative error on the largest real eigenvalue as a function of execution time, when using the spatial methods S and S_p (see text for the definition of abbreviations). Different execution times correspond to different discretization steps.

(2) Lorentzian potential

$$U(y) = A\frac{\Gamma/2}{(y-y_0)^2 + (\Gamma/2)^2} \tag{31}$$

with $y_0 = 200\,\mathrm{nm}$, $\Gamma = 100\,\mathrm{nm}$ and $A = 10\,\mathrm{eV\,nm}$

(3) Parabolic potential

$$U(y) = \bar{A}(y-\bar{y})^2 \tag{32}$$

with $\bar{y} = 250\,\mathrm{nm}$ and $\bar{A} = 0.2\,\mathrm{eV}/(250\,\mathrm{nm})^2$.

We set the electron injection energy to $E = 0.1\,\mathrm{eV}$ and study the scaling of the eigenvalue precision as a function of the execution time on an Intel Xeon CPU E5420 2.50GHz processor. Diagonalization is performed by means of standard LAPACK routines. In case (F), the coefficients h_n are computed on an extremely fine grid, independent of the dimension D of the truncated problem, without introducing any sizable overhead.

Figures refer to the maximum real eigenvalues. We did not find significant differences in the behavior of the other eigenvalues. However, eigenvalues associated with larger κ_x values converge faster to the corresponding eigenvalues of the original problem (16). This can be interpreted as a consequence of the fact that large κ_x values correspond to a small kinetic energy in the transverse direction (the total energy is constant), i.e., to transverse modes with large wavelength, which are less sensitive to the discretization or the frequency cutoff.

In Figs. 3 and 4 we report the relative error on the largest real eigenvalue for the two spatial approaches S and S_p (in Fig. 3), and the methods S_p and F (in Fig. 4) as a function of the execution time. The data points for different values of the execution time have been obtained by varying the discretization step in the case of the spatial methods, and varying the number of considered Fourier components in the case of the Fourier methods (the smaller the discretization step or the greater the number of Fourier components, the larger the execution time). Method (S_p) is slightly more efficient than method (S), probably due to the better block structure of the discretization matrix. However, in all the cases we have studied the Fourier methods largely outperform the direct space ones, often by several orders of magnitude.

Figure 4 also shows that the convergence of the Fourier method is strongly dependent on the shape and the analytic properties of the potential, which influence the number of Fourier coefficients needed to properly expand the eigenfunctions (and, in turn, the size of the matrices to be diagonalized).

The better performance of Fourier methods with respect to direct space ones has been recently noticed also in Ref. [53], where a Schrödinger equation with position dependent mass is considered. The authors used the following "Fourier-inspired" discretization for the derivative ($\mathcal{F}$ is the discrete Fourier transform and k is the reciprocal space variable)

$$\frac{d}{dx} \longrightarrow \mathcal{F}^{-1}\, k\, \mathcal{F} \tag{33}$$

and reported a convergence rate exponentially fast in the number of points of the discrete Fourier transform.

If we compare the numerical errors of the methods as a function of the size of the matrices involved in the analysis, we conclude that the errors deriving from the finite-difference discretization of the derivatives (and from the resulting distortion of the dispersion relation) turn out to be much larger than those related to the cutoff of the high-frequency Fourier components in the reciprocal space approach. This shows that, for the type of potentials we are interested in, the Fourier method is drastically more efficient than the others.

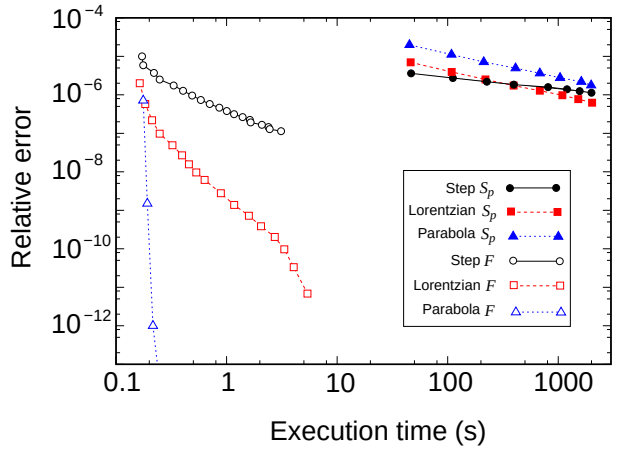


FIG. 4. (Color online) Relative error on the largest real eigenvalue as a function of the execution time. Comparison between the Fourier method and the spatial S_p one (see text for the definition of abbreviations). In the case of the parabolic potential the precision very quickly reaches the machine precision. Different execution times correspond to different values of the discretization step for the S_p method and to different numbers of components for the Fourier method.

VII. SOLUTION OF THE TRANSPORT PROBLEM

In the previous sections we have described numerical methods to compute the eigenvalues and the eigenfunctions of the Dirac equation in a longitudinally invariant ribbon. The total wave functions on the two sublattices $\psi_\beta(\vec{r})$ ($\beta = A, B$) are a linear combination of modes $\psi_{\beta i}(\vec{r})$ of the form:

$$\begin{aligned}\psi_{\beta i}(\vec{r}) &= \left[e^{-iKy}\Phi^{\vec{K}}_{\beta i}(y) - ie^{iKy}\Phi^{\vec{K}'}_{\beta i}(y)\right] e^{i\kappa_{xi}x} \\ &\equiv \chi_{\beta i}(y)\, e^{i\kappa_{xi}x}\ .\end{aligned} \tag{34}$$

In the case of a general potential $U(\vec{r})$ we divide the ribbon into a series of transverse slices, in such a way that within each slice the potential is approximately independent of x. For each slice we can then apply the previously discussed methods to estimate the modes $\psi_{\beta i}$ and their longitudinal momenta κ_x. At the interfaces between adjacent slices we have to enforce the continuity of the total wave function (the $\vec{k}\cdot\vec{p}$ approximation is reliable only if the potential varies slowly on the lattice scale, thus no δ-type potentials are allowed). We remark here a difference with respect to the standard Schrödinger case: the Dirac equation is a first-order differential equation, thus we do not have to impose the continuity of the normal derivative of the wave function.

Since the atomic orbitals in Eq. (1) are strongly localized, enforcing the continuity of the total wave function amounts to imposing the continuity of the wave functions on both inequivalent sublattices separately. Moreover, since the functions $\psi_\beta(\vec{r})$ have Fourier components localized around the two inequivalent Dirac points (which are significantly separated from each other), the continuity of the functions $\psi_\beta(\vec{r})$ implies also the continuity of the envelope functions F.

Integrating the probability current density in the x direction [32]

$$J_x(y) = v_F\left[\vec{F}^\dagger_{\vec{K}}(y)\sigma_x\vec{F}_{\vec{K}}(y) + \vec{F}^\dagger_{\vec{K}'}(y)\sigma_x\vec{F}_{\vec{K}'}(y)\right] \tag{35}$$

over the transverse section, and using Eq. (28), we can express the longitudinal probability current as follows:

$$\begin{aligned}I_x &= \int_0^{\tilde{W}} J_x(y)dy = 4v_F\tilde{W}\,\mathrm{Re}\left[\sum_{n=-D}^{D}(a^A_n)^* a^B_n\right] \\ &= v_F\int_0^{2\tilde{W}}\vec{\varphi}(y)^\dagger\sigma_x\vec{\varphi}(y)dy\,.\end{aligned} \tag{36}$$

From Eq. (18) we deduce that $(I_x)_{-\kappa_x} = -(I_x)_{\kappa_x}$, $(I_x)_{\kappa_x^*} = (I_x)_{\kappa_x}$ and $(I_x)_{-\kappa_x^*} = -(I_x)_{\kappa_x}$. In particular, if κ_x is purely imaginary, we have $I_x = 0$, i.e., modes with purely imaginary eigenvalues do not carry current. This is in general not true for eigenvalues that have at the same time a nonzero real and imaginary part. We classify the modes as right-moving or left-moving, depending on whether they have a positive or negative longitudinal probability current I_x. We also extend the definition of right-moving (left-moving) to the modes with $I_x = 0$ and $\mathrm{Im}(\kappa_x) > 0$ ($\mathrm{Im}(\kappa_x) < 0$).

In detail, in our simulation code we order the modes on the basis of the value of the corresponding κ_x. We first consider the real κ_x (arranged in order of decreasing modulus), then the complex ones, and finally the purely imaginary ones (sorted in order of increasing modulus). Since this ordering reflects the expected weight of the different modes in a transport simulation, in our computations we consider only the first n_{mod} right-moving modes and the first n_{mod} left-moving modes of each slice. Clearly n_{mod} has to be large enough for the final physical result to be insensitive to its specific value. Moreover, we select the modes in such a way as to preserve the $Z_2\times Z_2$ symmetry, which means to pick at the same time the modes with eigenvalues κ_x, $-\kappa_x$, κ_x^*, and $-\kappa_x^*$.

Let us now sketch the basic steps to compute the scattering matrix for a single discontinuity of the potential at the interface between adjacent slices. We denote by l/r the modes on the left/right of the discontinuity and by $+/-$ the right/left-moving modes. We use the index i to denote the mode impinging on the discontinuity, e.g., from the left. The wave function $\psi_\beta(\vec{r})$ on the left side can be written as

$$\chi^{l+}_{\beta i}(y)\, e^{i\kappa^{l+}_{xi}(x_{dis}-x_{in})} + \sum_n r_{ni}\chi^{l-}_{\beta n}(y)\, e^{i\kappa^{l-}_{xn}(x_{dis}-x_{in})}\ , \tag{37}$$

while on the right side it can be expressed in the form

$$\sum_n t_{ni}\chi^{r+}_{\beta n}(y)\, e^{i\kappa^{r+}_{xn}(x_{dis}-x_{out})}\ . \tag{38}$$

Here x_{in} and x_{out} are the longitudinal positions of the boundaries of the considered scattering region, x_{dis} is the position of the discontinuity, while r_{ni} and t_{ni} are the reflection and transmission coefficients. By continuity, functions (37) and (38) must be equal. An analogous relation can be established for a mode injected from the right. These continuity relations have to be enforced for both sublattices and for all the $2\,n_{mod}$ modes impinging from the left and from the right.

In order to evaluate all the $4\,n_{mod}^2$ reflection and transmission coefficients, we can project the $4\,n_{mod}$ continuity constraints onto a set of functions chosen in such a way as to obtain the correct number of independent equations. From Eq. (29) we have

$$\chi_{\beta i}(y) = 2\,i \sum_{n=-D}^{D} \left\{ a_n^{\beta i} \sin[(n-n_0)\pi y/\tilde{W}] \right\} , \qquad (39)$$

hence it is natural to project each continuity relation on the set of n_{mod} functions

$$S_j(y) = \sin\left((j-n_0)\pi y/\tilde{W} \right) , \qquad (40)$$

for $j = -(n_{mod}-1)/2, \ldots, (n_{mod}-1)/2$ (for the sake of simplicity n_{mod} is assumed odd). Since we consider values of n_{mod} such that $(n_{mod}-1)/2 < n_0$, these functions are linearly independent. It is simple to show that the matrix elements are

$$\langle S_j(y)|\chi_{\beta i}(y)\rangle = \int_0^{\tilde{W}} S_j^*(y)\chi_{\beta i}(y)dy = i\tilde{W}a_j^{\beta i} ; \qquad (41)$$

thus all the computations can be performed in the reciprocal space, avoiding the evaluation of the sums in Eq. (28).

Once the scattering matrices corresponding to the various interfaces have been computed, they can be composed according to the standard procedure (see, e.g., Ref. [54]) to obtain the total scattering matrix S of the ribbon:

$$S = \begin{pmatrix} r & \tilde{t} \\ t & \tilde{r} \end{pmatrix} \qquad (42)$$

Here r and t are the reflection and transmission matrices for the modes impinging from the left, $\tilde{r}$ and $\tilde{t}$ the corresponding matrices for the modes impinging from the right.

For practical purposes it is convenient to introduce the current form S' of the scattering matrix:

$$S' = \begin{pmatrix} r' & \tilde{t}' \\ t' & \tilde{r}' \end{pmatrix} , \qquad (43)$$

relating the "current amplitudes" instead of the "wave amplitudes" of the modes [54]. This matrix involves only the modes with $I_x \neq 0$ and its elements are given by $s'_{nm} = s_{nm}\sqrt{|I_{xn}|/|I_{xm}|}$, with $s = r, t, \tilde{r}, \tilde{t}$. As a result of current conservation, it can be shown that S' is unitary (see, e.g., Ref. [54]), which is a useful check to be performed at the end of the computations. In all our simulations we checked that numerical violations of the unitarity relation are less than 10^{-13}.

From S' we can compute the conductance of the ribbon

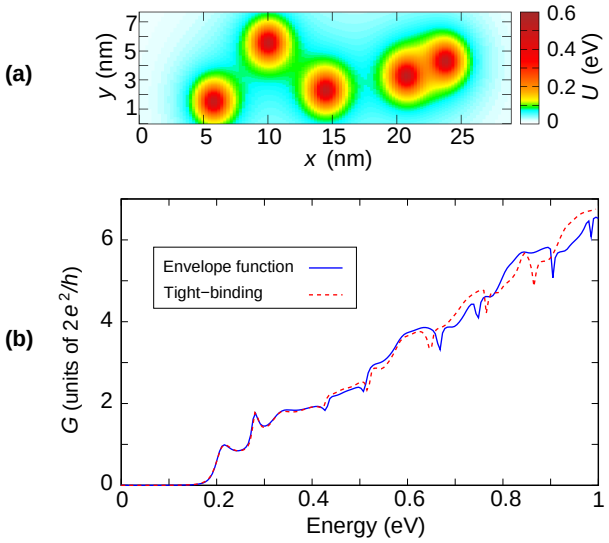


FIG. 5. (Color online) (a) Map of the potential in the nanoribbon, given by a superposition of Lorentzian functions. (b) Normalized conductance as a function of the injection energy, obtained within the envelope function and the nearest-neighbor semiempirical tight-binding approximations.

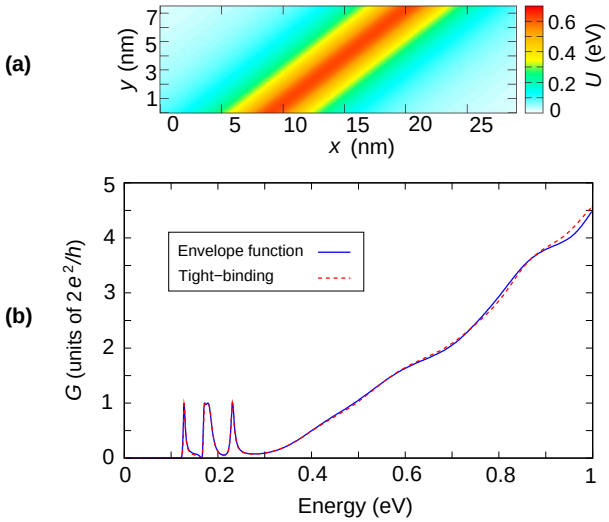


FIG. 6. (Color online) (a) Map of the potential in the nanoribbon, represented by a tilted barrier with a Lorentzian profile. (b) Normalized conductance as a function of the injection energy, obtained within the envelope function and the nearest-neighbor semiempirical tight-binding approximations.

by means of the Landauer-Büttiker formula

$$G = \frac{2\,e^2}{h} \sum_{n,m} |t'_{nm}|^2 \ , \tag{44}$$

where the sum runs over the modes with $I_x \neq 0$ in the first and last transverse regions of the ribbon.

In studies of unconfined graphene or of ribbons with large aspect ratio, it is usual to assume periodic instead of Dirichlet boundary conditions; the two Dirac points are then completely decoupled, and it is customary to solve the Dirac equation for just one valley and use a factor of four instead of two in Eq. (44). The physical Dirichlet boundary conditions introduce instead a coupling between the two inequivalent Dirac points, requiring the use of the more general formulation (44).

For validation purposes, we have performed a transmission calculation for a structure that is small enough to allow also a treatment with a standard tight-binding code (in particular we have used NanoTCAD ViDES) [55, 56]. We considered an armchair nanoribbon with 60 dimer lines ($\approx$ 7.5 nm wide), in the presence of two different realistic potential profiles.

In the first test case the electrostatic potential is a superposition of Lorentzian functions, and can schematically represent the effect on the ribbon of charged impurities located in the substrate on which graphene lies. In particular, we consider five Lorentzian functions, with a peak amplitude of 0.5 eV and a half-width at half-maximum equal to 0.64 nm (see Fig. 5(a)). In Fig. 5(b) we show the computed behavior of the conductance G (in units of $2e^2/h$) as a function of the injection energy, together with the corresponding results obtained with ViDES. We observe a very good agreement between the two different approaches in the low injection energy regime $E_{in} \lesssim 0.5$ eV, i.e., the one in which the envelope function method can be safely applied. For larger energies, the simple Dirac equation, which represents only a first-order $\vec{k} \cdot \vec{p}$ approximation, does not appropriately describe the physics of graphene any more, and thus discrepancies between the two results appear, even though the qualitative behavior of the conductance is well reproduced for all the explored injection energies.

The other potential profile we have considered is a barrier, tilted with respect to the ribbon edges and with a Lorentzian profile, with a peak amplitude of 0.625 eV and a half-width at half-maximum equal to 2 nm [see Fig. 6(a)]. The ribbon has a width of 60 dimer lines, as in the previous example. This potential can be the representation of the electrostatic effect at the graphene level of a biased gate or of a line of charge present at a certain distance from it. In Fig. 6(b) we report the behavior of G (in units of $2e^2/h$) as a function of the electron energy, obtained with our envelope-function-based calculation and with the tight-binding code. Also in this case we notice a good agreement between the two approaches, especially in the low-energies regime, in which the $\vec{k} \cdot \vec{p}$ approximation is expected to be more accurate.

Indeed, our numerical analysis is based on the use, in each section with longitudinally constant potential, of the continuum Dirac equation (5). This approximation is valid if the following conditions are satisfied:

(1) The dispersion relation is approximately linear

(2) The wave function is slowly varying on the scale of the lattice spacing

(3) The potential is slowly varying on the scale of the lattice spacing.

In the hypothesis of a slowly varying potential [57], the energy of an electron with wave vector $\vec{\kappa}$ in position $\vec{r}$ can be written as $E \simeq T(\vec{\kappa}) + U(\vec{r})$, where T is the kinetic energy. Observing the explicit form of $T(\vec{\kappa})$ (i.e., the actual dispersion relation in the absence of potential energy, a relationship which can be derived, for example, with a tight-binding formulation [30, 58]), we see that the first condition, i.e., the linear approximation for $T(\vec{\kappa})$ ($T(\vec{\kappa}) \simeq \pm\hbar v_F|\vec{\kappa}|$), is valid for $|T(\vec{\kappa})| \lesssim 1$ eV, which corresponds to

$$|E - U(\vec{r})| \lesssim 1 \text{ eV} \, . \tag{45}$$

The second condition can be expressed in the form $\lambda = 2\pi/|\vec{\kappa}| \gg a$ (where λ is the electron wavelength). Exploiting the relation (valid under the previous approximations) $E \simeq \pm\hbar v_F|\vec{\kappa}| + U(\vec{r})$, this inequality translates into the condition

$$|E - U(\vec{r})| \ll (2\pi\hbar v_F)/a \approx 15 \text{ eV} \, , \tag{46}$$

which is clearly weaker than Eq. (45).

Instead, the requirement on the smoothness of the potential (the third condition) introduces a limitation on the derivative of U along y (the only spatial variable along which U varies within each section). If we require the variation of the potential energy over the lattice constant a to be negligible with respect to γ_0 [which represents an order of magnitude of the energies involved, since, in a first approximation [58], $T(\vec{\kappa})$ has values between $-3\gamma_0$ and $3\gamma_0$], this further constraint can be expressed as

$$|\partial U/\partial y| \ll \gamma_0/a \approx 11 \text{ eV/nm} \, . \tag{47}$$

In the previous numerical examples, Eq. (47) was always well satisfied; thus the only limit to the application of the Dirac equation was the condition (45) on the injection energy. Indeed, as previously noted, for $E \gtrsim 0.5$ eV the continuum and the tight-binding results are not in as good an agreement as in the low-energy region.

VIII. CONCLUSIONS

We have presented a numerically efficient approach, including physical boundary conditions, for the evaluation of transport properties of graphene devices for which the

application of atomistic techniques is computationally prohibitive. We have focused on ribbons with armchair edges, which we modeled within a continuum, envelope function approximation.

For the computation of the transmission we have adopted a recursive scattering matrix approach, which requires the solution of a collection of Dirac equations in the presence of longitudinally constant potentials. We have shown that a reciprocal space approach is largely preferable with respect to the more commonly adopted finite difference methods, since it can reduce the computational cost of the procedure by orders of magnitude.

We have compared our results for structures small enough to allow an atomistic simulation with those obtained by means of tight-binding techniques, finding good agreement within the range of validity of the $\vec{k}\cdot\vec{p}$ approximation.

ACKNOWLEDGMENTS

It is a pleasure to thank Paolo Pintus for useful discussions.

APPENDIX: ALTERNATIVE FORMULATION

We present here a reformulation of Eq. (16) as a second order differential equation for a scalar function. Let $\xi(y)$ be defined by

$$\begin{aligned}\left[-\frac{d^2}{d\,y^2}+2i\,h(y)\frac{d}{d\,y}\right]\xi(y) &= -\kappa_x^2\xi(y)\\ \xi(2\tilde{W}) &= e^{2iK_0\tilde{W}}\xi(0)\\ \xi'(2\tilde{W}) &= e^{2iK_0\tilde{W}}\xi'(0)\end{aligned} \tag{A.1}$$

where $\xi'(y)$ is a shorthand for $d\xi/dy$ and K_0 is defined as

$$K_0 = K + \frac{1}{\tilde{W}}\int_0^{\tilde{W}} h(\alpha)d\alpha\,. \tag{A.2}$$

One can easily verify that system (16) is solved by

$$\vec{\varphi}(y) = e^{-i\int_0^y h(\alpha)d\alpha}\left[\kappa_x\xi(y)\begin{pmatrix}1\\ i\end{pmatrix} - \xi'(y)\begin{pmatrix}1\\ -i\end{pmatrix}\right]\,. \tag{A.3}$$

[1] K. S. Novoselov, A. K. Geim, S. V. Morozov, D. Jiang, Y. Zhang, S. V. Dubonos, I. V. Grigorieva, and A. A. Firsov, Science **306**, 666 (2004).
[2] M. I. Katsnelson and K. S. Novoselov, Solid State Commun. **143**, 3 (2007).
[3] A. K. Geim, Science **324**, 1530 (2009).
[4] G. Iannaccone, G. Fiori, M. Macucci, P. Michetti, M. Cheli, A. Betti, and P. Marconcini, in IEEE Int. Electron Device Meeting (IEDM), IEEE Conference Proceedings, 245 (2009), DOI: 10.1109/IEDM.2009.5424376.
[5] E. McCann and V. I. Fal'ko, Phys. Rev. Lett. **96**, 086805 (2006).
[6] T. Ohta, A. Bostwick, T. Seyller, K. Horn, and E. Rotenberg, Science **313**, 951 (2006).
[7] E. V. Castro, K. S. Novoselov, S. V. Morozov, N. M. R. Peres, J. M. B. Lopes dos Santos, J. Nilsson, F. Guinea, A. K. Geim, and A. H. Castro Neto, Phys. Rev. Lett. **99**, 216802 (2007).
[8] Y. Zhang, T.-T. Tang, C. Girit, Z. Hao, M. C. Martin, A. Zettl, M. F. Crommie, Y. R. Shen, and F. Wang, Nature (London) **459**, 820 (2009).
[9] Y. Ouyang, Y. Yoon, and J. Guo, in IEEE Int. Electron Device Meeting (IEDM), Tech. Dig., 4796739 (2008), DOI: 10.1109/IEDM.2008.4796739.
[10] T. J. Echtermeyer, M. C. Lemme, M. Baus, B. N. Szafranek, A. K. Geim, and H. Kurz, IEEE Electron Device Lett. **29**, 952 (2009).
[11] D. C. Elias, R. R. Nair, T. M. G. Mohiuddin, S. V. Morozov, P. Blake, M. P. Halsall, A. C. Ferrari, D. W. Boukhvalov, M. I. Katsnelson, A. K. Geim, and K. S. Novoselov, Science **323**, 610 (2009).
[12] D. W. Boukhvalov and M. I. Katsnelson, J. Phys.: Condens. Matter **21**, 344205 (2009).
[13] P. Marconcini, A. Cresti, F. Triozon, G. Fiori, B. Biel, Y.-M. Niquet, M. Macucci, and S. Roche, ACS Nano **6**, 7942 (2012).
[14] P. Marconcini, A. Cresti, F. Triozon, G. Fiori, B. Biel, Y.-M. Niquet, M. Macucci, and S. Roche, in Proceedings of IWCE 2012, IEEE Conference Proceedings, 6242844 (2012), DOI: 10.1109/IWCE.2012.6242844.
[15] Y.-B. Tang, L.-C. Yin, Y. Yang, X.-H. Bo, Y.-L. Cao, H.-E. Wang, W.-J. Zhang, I. Bello, S.-T. Lee, H.-M. Cheng, and C.-S. Lee, ACS Nano **6**, 1970 (2012).
[16] D. Wei, Y. Liu, Y. Wang, H. Zhang, L. Huang, and G. Yu, Nano Lett. **9**, 1752 (2009).
[17] K. S. Novoselov, V. I. Fal'ko, L. Colombo, P. R. Gellert, M. G. Schwab, and K. Kim, Nature (London) **490**, 192 (2012).
[18] F. Schwierz, Nature Nanotech. **5**, 487 (2010).
[19] A. N. Mina and A. H. Phillips, J. Appl. Sci. Res. **9**, 1854 (2013).
[20] E. W. Hill, A. Vijayaragahvan, and K. Novoselov, IEEE Sensors J. **11**, 3161 (2011).
[21] F. Bonaccorso, Z. Sun, T. Hasan, and A. C. Ferrari, Nature Photon. **4**, 611 (2010).
[22] F. Xia, T. Mueller, Y.-m. Lin, A. Valdes-Garcia, and Phaedon Avouris, Nature Nanotech. **4**, 839 (2009).
[23] D. R. Cooper, B. D'Anjou, N. Ghattamaneni, B. Harack, M. Hilke, A. Horth, N. Majlis, M. Massicotte, L. Vandsburger, E. Whiteway, and V. Yu, ISRN Condensed Matter Physics **2012**, 501686 (2012), DOI: 10.5402/2012/501686.
[24] N. M. R. Peres, Rev. Mod. Phys. **82**, 2673 (2010).
[25] R. Danneau, F. Wu, M. F. Craciun, S. Russo, M. Y. Tomi, J. Salmilehto, A. F. Morpurgo, and P. J. Hakonen, Phys. Rev. Lett. **100**, 196802 (2008).
[26] A. A. Balandin, Nature Nanotech. **8**, 549 (2013).
[27] J. Wurm, M. Wimmer, I. Adagideli, K. Richter, and H. U. Baranger, New J. Phys. **11**, 095022 (2009).

[28] H. Li, L. Wang, Z. Lan, and Y. Zheng, Phys. Rev. B **79**, 155429 (2009).

[29] B. Zhou, B. Zhou, W. Liao, and G. Zhou, Phys. Lett. A **374**, 761 (2010).

[30] A. H. Castro Neto, F. Guinea, N. M. R. Peres, K. S. Novoselov, and A. K. Geim, Rev. Mod. Phys. **81**, 109 (2009).

[31] L. Brey and H. A. Fertig, Phys. Rev. B **73**, 235411 (2006).

[32] P. Marconcini, M. Macucci, La Rivista del Nuovo Cimento **34**, 489 (2011), DOI: 10.1393/ncr/i2011-10068-1.

[33] J. H. Bardarson, J. Tworzydło, P. W. Brouwer, and C. W. J. Beenakker, Phys. Rev. Lett. **99**, 106801 (2007).

[34] K. Nomura, M. Koshino, and S. Ryu, Phys. Rev. Lett. **99**, 146806 (2007).

[35] J. Tworzydło, C. W. Groth, and C. W. J. Beenakker, Phys. Rev. B **78**, 235438 (2008).

[36] R. Stacey, Phys. Rev. D **26**, 468 (1982).

[37] C. M. Bender, K. A. Milton, and D. H. Sharp, Phys. Rev. Lett. **51**, 1815 (1983).

[38] A. R. Hernández and C. H. Lewenkopf, Phys. Rev. B **86**, 155439 (2012).

[39] L. Susskind, Phys. Rev. D **16**, 3031 (1977).

[40] I. Snyman, J. Tworzydło, and C. W. J. Beenakker, Phys. Rev. B **78**, 045118 (2008).

[41] J. T. Chalker and P. D. Coddington, J. Phys. C **21**, 2665 (1988).

[42] C.-M. Ho and J. T. Chalker, Phys. Rev. B **54**, 8708 (1996).

[43] M. R. Connolly, R. K. Puddy, D. Logoteta, P. Marconcini, M. Roy, J. P. Griffiths, G. A. C. Jones, P. A. Maksym, M. Macucci, and C. G. Smith, Nano Lett. **12**, 5448 (2012).

[44] D. Logoteta, P. Marconcini, M. R. Connolly, C. G. Smith, and M. Macucci, in Proceedings of IWCE 2012, IEEE Conference Proceedings, 6242841 (2012), DOI: 10.1109/IWCE.2012.6242841.

[45] The Chalker-Coddington model of Ref. [40] describes just one valley of the graphene spectrum, so it is impossible to implement in it the physical boundary conditions.

[46] M. Fagotti, C. Bonati, D. Logoteta, P. Marconcini, and M. Macucci, Phys. Rev. B **83**, 241406(R) (2011).

[47] T. Ando, J. Phys. Soc. Jpn. **74**, 777 (2005).

[48] H. J. Rothe, *Lattice Gauge Theories: An Introduction*, World Scientific Lecture Notes in Physics 74 (World Scientific, Singapore, 2005).

[49] I. Montvay and G. Münster, *Quantum Fields on a Lattice* (Cambridge University Press, Cambridge, 1994).

[50] A. Smilga, *Lectures on Quantum Chromodynamics* (World Scientific, Singapore, 2001).

[51] C. Bonati and M. Fagotti (unpublished).

[52] T. W. Körner, *Fourier Analysis* (Cambridge University Press, Cambridge, 1988).

[53] J. Förster, A. Saenz, and U. Wolff, Phys. Rev. E **86**, 016701 (2012).

[54] S. Datta, *Electronic Transport in Mesoscopic Systems* (Cambridge University Press, Cambridge, 1995).

[55] http://vides.nanotcad.com

[56] G. Fiori and G. Iannaccone, Proc. IEEE **101**, 1653 (2013).

[57] N. W. Ashcroft and N. D. Mermin, *Solid State Physics* (Thomson Learning, London, 1976), p. 341.

[58] R. Saito, G. Dresselhaus, and M. S. Dresselhaus, *Physical Properties of Carbon Nanotubes* (Imperial College Press, London, 1998).